Location and Properties of the Taxol Binding Center in Microtubules: A Picosecond Laser Study with Fluorescent Taxoids†

M[a] Pilar Lillo,* Olga Cañadas,‡ Robert. E. Dale,§ and A. Ulises Acuña

Instituto de Química-Física Rocasolano, CSIC, Serrano 119, 28006 Madrid, Spain

Received May 22, 2002; Revised Manuscript Received August 20, 2002

ABSTRACT: The interaction of two bioactive, fluorescent analogues of the anticancer drug Taxol, Flutax1 [7-*O*-[*N*-(fluorescein-4′-carbonyl)-L-alanyl]taxol] and Flutax2 [7-*O*-[*N*-(2,7-difluorofluorescein-4′-carbonyl)-L-alanyl]taxol], with microtubules in solution has been studied with picosecond laser methods. As shown here, although a mixture of the fluorescein mono- and dianion species of Flutax1 is present in solution, the *bound* taxoid contains only the dianion form of the dye. This indicates strong electrostatic interactions at the microtubule lattice with the appending dye, most likely with charged residues of the M-loop of the β-tubulin subunit. Moreover, analysis of the dynamic depolarization of microtubule-bound Flutax at low binding site occupancy was consistent with a protein active center with significant conformational flexibility. On the other hand, for microtubules fully saturated with the taxoid, a new, additional depolarizing process was observed, with relaxation times of 14 ns (Flutax1) and 8 ns (Flutax2), which is due to Förster resonance energy *homo*transfer (FREHT) between neighboring dye molecules. Application of a detailed analysis of FREHT-induced depolarization in a circular array of dye molecules presented here yielded a separation between nearest-neighbor Flutax moieties of 40 ± 5 Å, for microtubules made up of between 12 and 14 protofilaments, a value that is only compatible with the Taxol binding site being located at the inner wall of the microtubule. The internal position of the drug molecular target as measured here is also consistent with other spectroscopic observations and confirms existing predictions based on microtubule structures modeled from high-resolution, electron density maps of $\alpha\beta$-tubulin.

Microtubules (MT)[1] are long (>1 μm), thin (~26 nm) hollow cylindrical polymers of tubulin that play a critical role in mitosis, signaling, transport, and motility of eukaryotic cells (*1*). The MT wall is organized from linear strings, *protofilaments*, of $\alpha\beta$-tubulin heterodimers (2×50000 M_r) arranged in a porous lattice (*2*−*4*). The microtubule assembly involves two types of attractive contacts between tubulin subunits: head-to-tail interaction of heterodimers to form the protofilament and lateral association of protofilaments (Figure 1), the first being much stronger than the second (*3*, *5*).

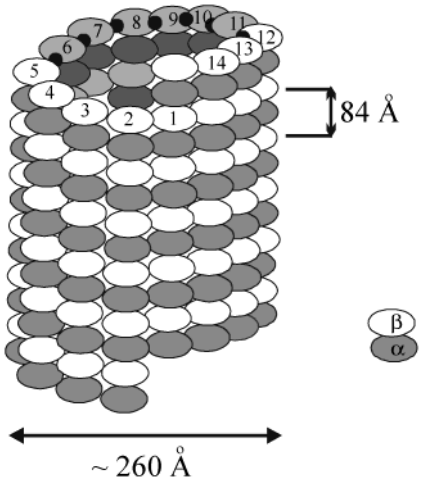

FIGURE 1: Schematic representation of a 14-protofilament microtubule as a regular helix built of heterodimers of $\alpha\beta$-tubulin. Taxoid molecules in possible binding sites in the inter-protofilament region at the inner surface of the microtubule are represented as small filled circles. Each protofilament is slightly longitudinally shifted with respect to its neighbor (~9 Å), giving rise to the helical path around the microtubule surface traced by the binding sites. This vertical shift, together with the somewhat variable number of protofilaments (12−14), generates a family of different microtubule surface lattices, with protofilaments running from parallel to the long axis of the microtubule to being slightly skewed.

† This work was financed by Grants PB96-852 and BQU/2000-1500 from the Spanish Dirección General de Enseñanza Superior e Investigación (DGESI). R.E.D. was supported by The British Council and DGESI Grants and O.C. by a fellowship from the DGESI. The laser system was purchased with special grants from the CSIC and the DGESI (AE-1996).

* To whom correspondence should be addressed. Phone: +34-915619400. Fax: +34-915642431. E-mail: pilar.lillo@iqfr.csic.es.

‡ Present address: Departamento de Bioquímica y Biología Molecular I. Fac. Biología, Universidad Complutense de Madrid, Madrid, Spain.

§ Present address: The Randall Centre, King's College London, GKT School of Biomedical Sciences, New Hunt's House, Guy's Hospital Campus, London SE1 1UL, U.K.

[1] Abbreviations: Taxol (registered trademark of Bristol-Myers Squibb, Inc.), paclitaxel; Flutax1, 7-*O*-[*N*-(fluorescein-4′-carbonyl)-L-alanyl]taxol; Flutax2, 7-*O*-[*N*-(2,7-difluorofluorescein-4′-carbonyl)-L-alanyl]taxol; Flu1-Ala, *N*-(fluorescein-4′-carbonyl)-L-alanine methyl ester; GTP, guanosine 5′-triphosphate; GDP, guanosine 5′-diphosphate; EGTA, ethylene glycol bis(β-aminoethyl ether)-*N*,*N*,*N*′,*N*′-tetraacetic acid; PEGTA buffer, 10 mM sodium phosphate, 1 mM EGTA, 1 mM GTP, 6 mM $MgCl_2$, and 3.4 M glycerol, pH 6.5−9.0; PEDTA buffer, 10 mM sodium phosphate, 1 mM EDTA, 1 mM GDP, and 7 mM $MgCl_2$, pH 6.6; FREHT, Förster resonance energy homotransfer; TB, $\alpha\beta$-tubulin; MT, microtubules.

10.1021/bi0261793 CCC: $22.00
Published on Web 10/08/2002

Scheme 1

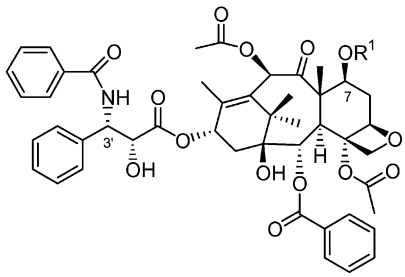

	R^1	R^2
Taxol	H	
Flutax1	CO-CH(Me)-NHCO-**flu**	H
Flutax2	CO-CH(Me)-NHCO-**flu**	F

MeOCO-CH(Me)-NHCO-**flu** (R_2 = H)
Flu1Ala

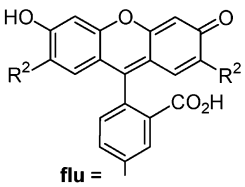

flu =

The average number of protofilaments, *N*, in living cell MT is frequently fixed at 13 by the microtubule organizing centers (*6*), while in MT assembled in solution from purified tubulin, *N* can take values from 10 to 16, depending on the polymerization conditions (*7a*, *8*). Nevertheless, the contacts between tubulin subunits of adjacent protofilaments (lateral interactions) remain virtually unchanged in all of these MT polymorphs, because small rotations of the wall lattice suppress the expected mismatches (*7a*, *9*−*11*). The lateral interactions can be either between homologous subunits (αα, *ββ*: B-type lattice) or heterologous subunits (α*β*: A-type lattice), most microtubules seeming to comprise a mixture of A- and B-forms, with the latter predominant (*7b*).

Cell microtubules are specific targets of an expanding series of drugs, of which the natural diterpene Taxol[1] (paclitaxel, Scheme 1) (*12*, *13*) has been introduced for the therapy of several carcinoma lines with great success (*14*, *15*). Although Taxol does not interact appreciably with free tubulin, the drug binds to MT with high affinity ($K_d \sim 10^{-8}$ M) and a maximum stoichiometry of 1 ligand per α*β*-tubulin heterodimer (*16*−*18*). Microtubules assembled in solution in the presence of Taxol contain 12 protofilaments on the average, but this number increases to 14 in the case of docetaxel, a structurally related analogue (*4*, *8*). Photoaffinity labeling experiments (*19*−*21*), high-resolution structures of tubulin from electron crystallography of zinc sheets (*22*), and the reconstruction of microtubules based on this structure (*3*, *4*) locate the site of Taxol recognition in the *β*-tubulin subunit, close to the inner wall of the microtubule and near the lateral contact surface between protofilaments. In contrast, with this view of the drug binding site hidden in the interior of the narrow MT, earlier observations noted a fast rate of incorporation of Taxol to the microtubule from solution (*18*, *23*).

Fluorescent analogues of Taxol have been of utility in unraveling the cellular targets of the drug (*24*) and, when the resulting spectral changes are properly characterized, may provide details at the molecular level of its interaction with MT that cannot be obtained by other methods. Several fluorescent taxoids have been obtained (see, e.g., refs *25*−*28* and references cited therein), and of those introduced by this laboratory (*25*), we selected for the work presented here the analogues Flutax1[1] and Flutax2[1] (Scheme 1). These highly fluorescent derivatives contain a fluorescein-alanyl and a difluorofluorescein-alanyl substituent, respectively, at the nonessential position C-7 and compete with Taxol for the same binding site at all levels of organization (cells, isolated cytoskeletons, microtubule suspensions) with comparable affinity (*29*), a property that has been exploited in studies of structure−activity relationships (*30*).

It was shown in whole cells that the primary targets of Flutax1, as well as of the parent drug, are the centrosome and spindle-pole microtubules (*24*). In buffer solutions, these analogues adopt the same conformation (*31*) and interact with microtubules with identical stoichiometry (1:1) and similar binding strength ($K_d \sim 10^{-8}$ M) as Taxol (*29*, *32*). Finally, MT saturated with Flutax1 have been found to contain, on the average, 14.3 protofilaments (*32*).

The rate of incorporation of Taxol into its binding site in MT has also been addressed recently using Flutax, by stopped-flow techniques (*32*). In this study, it was concluded that, since the emitting taxoids interact initially at a very high rate (time constants of milliseconds), the binding site should be directly accessible, in contrast with a location facing the MT lumen as proposed by Nogales and co-workers (3).

Here, we report a study of the interaction of Flutax1 and Flutax2 with microtubules in solution at the molecular level, by picosecond time-resolved fluorescence intensity and depolarization techniques, that presents a quantitative description of our preliminary, low time resolution observations (*29*), and new structural and dynamic properties of the taxoid−MT system. In addition, we have undertaken resonance energy transfer experiments to determine the location of the Flutax probes in the MT structure. Energy transfer experiments between isolated pairs of *unlike* fluorophores bound to MT have been reported before (e.g., in ref *28*) from which the mean distance between fluorescent taxoid and colchicin analogues could be determined. However, in the present work we determine the relative position of the taxoids from the transfer between *identical* Flutax molecules bound to the MT surface. For this purpose a Förster resonance energy homotransfer (FREHT) model was developed, which idealizes the microtubule lattice as a series of stacked 14-membered α*β*-tubulin heterodimers symmetrically arranged as hollow rings. The bound taxoid molecules in each ring, at saturation of sites, are thus considered as cylindrically symmetrically distributed around the circumference of a ring of radius reflecting the location of their binding site to *β*-subunits. At the level of resolution of the method, this simplified model adequately corresponds with an average of possible microtubule lattices. The Flutax−Flutax distance estimated in this way and reported here is consistent only with a Taxol binding center located very close to the inner microtubule wall.

THEORY

Superposition of Depolarizing Processes. The time dependence of depolarization of fluorescence observed in

isotropic solutions of fluorophores brought about by successive independent processes can be characterized by a series of depolarizing factors (*33*, *34*):

$$d_j(t) = \frac{3}{2}\langle \cos^2 \theta_j(t)\rangle - \frac{1}{2} \quad (1)$$

the product of which is the well-known emission anisotropy, $r(t)$ (*35*). For a free fluorophore (F) in solution, rotating effectively as a sphere on a time scale comparable with or longer than that of fluorescence, the time-dependent depolarization factor is a simple exponential decay:

$$r_F(t) = r_0 d_F(t) = r_0 \exp\left[-\frac{t}{\phi_F}\right] \quad (2)$$

where r_0 is the intrinsic anisotropy and ϕ_F is the correlation time for free rotation of the fluorophore in solution (*36*).

In the case of Flutax, the fluorescein label (L) is attached by a number of rotatable bonds to the larger taxoid frame (T), and therefore, some hindered oscillation with respect to that frame may occur in solution, at rates faster than the isotropic tumbling of the fluorescein−taxoid complex (T) as a whole. In this case, the overall depolarization is well approximated by

$$r_T(t) = r_0 d_{L(T)}(t) d_T(t) = r_0\left\{(1 - {P_{2L}}^2)\exp\left[-\frac{t}{\phi_L}\right] + {P_{2L}}^2\right\}\exp\left[-\frac{t}{\phi_T}\right] \quad (3)$$

where $d_T(t)$ is the depolarization factor for the overall free rotation of the taxoid as a whole and $d_{L(T)}(t)$ that for the hindered motion of the label with respect to the taxoid (*34*). P_{2L} is the Legendre polynomial of rank 2 for the restricted angular motion of the fluorophore with respect to the taxoid:

$$P_{2L} = \frac{3}{2}\langle \cos^2 \theta_L\rangle - \frac{1}{2} \quad (4)$$

The designation L emphasizes that the hindered rotational correlation time ("wobbling") of the covalently bound dye with respect to the taxoid frame is not expected to correspond to the unhindered rotational correlation time of the free fluorophore under the same solution conditions: $\phi_L \leq \phi_F$.

When the taxoid is itself bound to the microtubule, which is immobile on the time scale of fluorescence, restriction of rotation of the taxoid with respect to the microtubule is described by the depolarization factor $d_{T(M)}(t)$, which is entirely analogous to that for restriction of the fluorophore with respect to the taxoid, leading to an overall depolarization of the emission from an isolated microtubule-bound taxoid, i.e., at low enough binding ratios (f) of fluorophore to the microtubule, formally described by

$$r_M(t)(f\rightarrow 0) = r_0 d_{L(T)}(t) d_{T(M)}(t) = r_0\left\{(1 - {P_{2L}}^2)\times \exp\left[-\frac{t}{\phi_L}\right] + {P_{2L}}^2\right\}\left\{(1 - {P_{2T}}^2)\exp\left[-\frac{t}{\phi_T}\right] + {P_{2T}}^2\right\} \quad (5)$$

Although eq 5 applies formally, it should be noted (a) that, analogously to the case for dye linked to Taxol, the wobbling correlation time for the taxoid bound to the microtubule, still designated ϕ_T here, is not expected to be the same as the correlation time for the taxoid as a whole when free under the same solution conditions, and (b) that the P_{2L} and ϕ_L appearing here are not necessarily the same as those for the fluorophohore linked to the taxoid when free in solution; both may be changed due to changes in molecular conformation of the taxoid−fluorophore complex on binding, as well as by further restrictions imposed by the structure of the binding site on the reorientational range of the pendant fluorophore.

When the microtubule-bound fluorescent taxoid saturates the binding sites, which are regularly spaced around the microtubule in a shallow helix (Figure 1), neighboring pairs around the helix may be close enough together for spectroscopic ruling (*37*) by Förster long-range resonance energy transfer (vide infra) to take place between the like fluorophores. Under these conditions, the further depolarization thus introduced can be represented by a third depolarization factor $d_{ET}(t)$, leading to a final overall emission anisotropy in the presence of homogeneous energy transfer in such a saturated system given, at least approximately, by

$$r_M(t)(f\rightarrow 1) = r_0 d_{L(T)}(t) d_{T(M)} d_{ET}(t) = r_0\left\{(1 - {P_{2L}}^2)\times \exp\left[-\frac{t}{\phi_L}\right] + {P_{2L}}^2\right\}\left\{(1 - {P_{2T}}^2)\exp\left[-\frac{t}{\phi_T}\right] + {P_{2T}}^2\right\}\left\{(1 - {P_{2ET}}^2)\exp\left[-\frac{t}{\langle\phi_{ET}\rangle}\right] + {P_{2ET}}^2\right\} \quad (6)$$

where $\langle\phi_{ET}\rangle$ is an effective average correlation time for the energy transfer depolarization, which is brought about by the difference in absolute orientation of those initially excited fluorophores which emit, from those excited indirectly via energy transfer (see Appendix). This additional mechanism of depolarization does not affect the values of P_{2L}, ϕ_L, P_{2T}, or ϕ_T as compared with those appearing in eq 5, which is relevant to isolated binding sites found at labeling ratios low enough to render the probability of finding adjacent sites occupied so negligible that no appreciable energy transfer is observed.

In eq 6 no restriction is placed on the value of $\langle\phi_{ET}\rangle$ relative to those of ϕ_L and ϕ_T. In the present case, however, as will be seen, the time scales for each depolarization event are well separated, such that $\phi_L \ll \phi_T \ll \langle\phi_{ET}\rangle$. Under these conditions, eq 5 for low binding ratios of fluorophore to the microtubule becomes well represented by

$$r_M(t)(f\rightarrow 0) \approx r_0\left((1 - {P_{2L}}^2)\exp\left[-\frac{t}{\phi_L}\right] + {P_{2L}}^2\left\{(1 - {P_{2T}}^2)\exp\left[-\frac{t}{\phi_T}\right] + {P_{2T}}^2\right\}\right) \quad (7)$$

while eq 6 for saturation of binding similarly becomes

$$r_M(t)(f\rightarrow 1) \approx r_0\left\{(1 - {P_{2L}}^2)\exp\left[-\frac{t}{\phi_L}\right] + {P_{2L}}^2\left((1 - {P_{2T}}^2)\exp\left[-\frac{t}{\phi_T}\right] + {P_{2T}}^2\left\{(1 - {P_{2ET}}^2)\times \exp\left[-\frac{t}{\langle\phi_{ET}\rangle}\right] + {P_{2ET}}^2\right\}\right)\right\} \quad (8)$$

It is seen that, within the given approximation, the first two exponential terms in eq 8 correspond exactly to those appearing in eq 7 for the low-binding regime. We note that, in this approximation, the anisotropy decays can be seen as a series of restricted reorientations in different time regimes for which the long-time limiting anisotropy in each regime becomes the "zero-point" anisotropy in the next, schematically:

$$r_0 \equiv r_{0L} \downarrow r_{\infty L} = r_0 P_{2L}^2 \equiv r_{0T} \downarrow r_{\infty T} = r_0 P_{2L}^2 P_{2T}^2 \equiv r_{0ET} \downarrow r_{\infty ET} = r_0 P_{2L}^2 P_{2T}^2 P_{2ET}^2.$$

Details of the theory of Förster energy transfer as applied to the taxoid−microtubule system are given in the Appendix.

MATERIALS AND METHODS

Materials

The fluorescent taxoids Flutax1[1] and Flutax2[1] (Scheme 1) were obtained by the reaction of 7-*O*-(L-alanyl)taxol with the corresponding amine-reactive fluorescent dye, as described by Souto and co-workers (*25*). The inactive derivative fluorescein-alanine (Flu1-Ala),[1] used for control experiments, was prepared as detailed elsewhere (*29*), and the docetaxel sample was from Rhône-Poulenc Rorer, Antony, France. Disodium fluorescein, from Sigma Chemical Co., was shown to be pure by thin-layer chromatography (*38*). The buffers used in the spectroscopic experiments were PEGTA [10 mM sodium phosphate, 1 mM EGTA, 1 mM GTP, 6 mM $MgCl_2$, 3.4 M glycerol, $\eta = 1.5$ cP (37 °C), pH 6.5−9.0] and PEDTA (10 mM sodium phosphate, 1 mM EDTA, 1 mM GDP, 7 mM $MgCl_2$, pH 6.6).

Methods

Sample Preparation. The solutions of purified tubulin, containing either two molecules of guanosine 5′-triphosphate (GTP) nucleotide per heterodimer (TB-GTP) or one GTP and one GDP molecule (TB-GDP), were prepared from calf brain as described elsewhere (*39*). These solutions were used to obtain two different microtubule preparations. MT-I: microtubules were assembled from TB-GTP in PEGTA buffer, pH 6.5, by raising the temperature to 37 °C for 1 h and then adding the fluorescent taxoid at 1:1, 1:10, 1:100, and 1:1000 taxoid:tubulin molar mixing ratios. Alternatively, the fluorescent taxoid could be added before assembly. MT-II: microtubules were assembled from TB-GDP in PEDTA buffer, pH 6.6, in the presence of the fluorescent taxoid at a 1:1 taxoid:tubulin molar mixing ratio by raising the temperature to 37 °C for 1 h (*29*). The overall $\alpha\beta$-tubulin heterodimer concentration in MT-I and MT-II preparations was usually 20 μM.

Spectroscopic Measurements. Absorbance spectra were recorded on a Cary 3E UV−Vis spectrophotometer. Corrected steady-state fluorescence excitation, emission, and anisotropy spectra were obtained on an SLM 8000D spectrofluorometer, using 300 μL samples in 5 × 5 mm path-length cuvettes. Fluorescence quantum yields were determined by reference to a solution of disodium fluorescein in 0.01 M NaOH, $\Phi = 0.93 \pm 0.03$ (*40*, *41*).

Time-resolved fluorescence intensity and depolarization measurements were performed by the time-correlated single-photon counting technique. The excitation light source was a Ti-sapphire picosecond laser (Tsunami, Spectra Physics, Mountain View, CA), pumped with a 5 W Nd:YVO_4 diode laser (Millennia, Spectra Physics), and associated with a second harmonic generator. Pulses of 1−2 ps width were used with a repetition rate of 0.8−4 MHz and ∼20 μW of average power at the samples. The linear polarization of the laser pulses was selected with a Berek compensator (Model 5540, New Focus) and a Glan-Taylor prism. The fluorescence collected in the horizontal plane, at 90° to the excitation beam, was focused on a monochromator ($f = 100$ mm, 8 nm bandwidth) through a cutoff filter, a motorized Glan-Taylor polarizer, and a quartz depolarizer (Acton Research Co.), and finally detected with a R1564U-06 microchannel plate (Hamamatsu). The detector pulses were amplified (Phillips Scientific 6954, ×50) and fed to counting electronics consisting of Tennelec 453 discriminators, an ORTEC 457 time-to-amplitude converter, and an Accuspec B (Canberra) pulse amplitude analyzer. A fast PIN diode (Hamamatsu S5973) focused on the fundamental laser beam produced the synchronization signal. Data were stored in 2−4 K channels, with a resolution of 6−13.1 ps/channel, up to 10^4 counts in the peak channel (∼5×10^6 total counts). The instrument response function was recorded as excitation light scattered from distilled water and could be optimized down to the detector limit (∼70 ps). The experimental samples (120 μL) were placed in thermostated, 3 × 3 mm path-length cuvettes and mixed regularly.

The decay of the total fluorescence intensity, $I(t) = I_m(t)$, was recorded with the emission polarizer set at the magic angle ($m = 54.7°$) relative to the vertically polarized excitation beam. The two components of the fluorescence, polarized parallel $I_{vv}(t)$ and perpendicular $I_{vh}(t)$ to the plane of polarization of the excitation beam, were recorded sequentially by alternating the orientation of the emission polarizer every 2 min. The experimentally recorded anisotropy $R(t)$ is related to the experimental emission decay by

$$R(t) = [I_{vv}(t) - GI_{vh}(t)]/[I_{vv}(t) + 2GI_{vh}(t)] \qquad (9)$$

where G is a scaling factor that accounts for differences in accumulation times and the detection efficiency for the two polarized intensities. The G factor was determined by normalizing the total number of counts under the time-resolved traces to match the value of the steady-state anisotropy of the samples separately measured (*42*), and varied between 0.9 and 1.1. Additional potential sources of error in the anisotropy that are not corrected by G may come from the scattering and birefringence (*43*) of the microtubule suspensions. For the samples used here the anisotropy was independent of the microtubule concentration, indicating that any scattering contribution was very low (*43*). On the other hand, it is well-known (*44*) that individual microtubules are birefringent, due to their large aspect ratio (length/width), although tubulin exhibits only very small intrinsic birefringence, if any (*45*). This effect was found to be negligible, probably due to the low microtubule concentration, small cuvette size, and frequent mixing of the suspensions.

Overlap Integral and Förster Radius R_0. The characteristic Förster radii for Flutax1 and Flutax2 "self"-transfer were obtained from the relevant overlap integrals calculated as

$$J = \frac{\sum_i \epsilon_m(\lambda_i) F(\lambda_i) \lambda^4}{\sum_i F(\lambda_i)} \qquad (\mathrm{M^{-1}\,cm^{-1}\,nm^4}) \qquad (10)$$

leading to

$$R_0 = 0.211(n^{-4}\Phi_D\langle\kappa^2\rangle J)^{1/6} = \left(\frac{3}{2}\langle\kappa^2\rangle\right)^{1/6} R_{2/3} \qquad (\text{Å}) \quad (11)$$

where Φ_D is the donor fluorescence quantum yield, $R_{2/3}$ the (usually quoted) Förster radius for $\langle\kappa^2\rangle = {}^2/_3$, and a value of 1.4 was taken for the refractive index, n ($n_{\mathrm{buffer,37°C}} = 1.37$, $n_{\mathrm{protein}} \approx 1.4$).

Analysis of Fluorescence Lifetimes and Anisotropy Decay. The decay of the total fluorescence intensity was fitted to a sum of $\boldsymbol{n}$ exponential functions ($\boldsymbol{n} = 1, 2$) by iterative convolution, using nonlinear least-squares global methods from the GLOBALS Unlimited (Urbana, IL) (*46*) general purpose program. The anisotropy decay function $r(t)$ was determined by simultaneous analysis of the two polarized components of the fluorescence intensity, using the same routines. In this case, the analysis consisted in finding the $r(t)$ numerical parameters that best fit the two polarized decay functions $i_{vv}(t) = [i(t)/3][1 + 2r(t)]$ and $i_{vh}(t) = [i(t)/3][1 - r(t)]$, where $i(t) = i_{vv}(t) + 2i_{vh}(t) = 3i_m(t)$, to the experimental traces $I_{vv}(t)$ and $I_{vh}(t)$, on introducing the lifetime obtained from magic-angle data as a fixed parameter. The adequacy of the analyses was determined from the reduced weighted sum of squares of residuals and visual inspection of the distribution of weighted residuals. The general expression used for the anisotropy decay fitting was

$$r(t) = r_0\left(\sum_{i=1}^{3}\beta_i \exp\left[-\frac{t}{\phi_i}\right] + \beta_\infty\right) \qquad (12)$$

where ϕ_i are correlation times, and the preexponential factors β_i and constant β_∞ are normalized amplitudes ($\sum_{i=1}^{3}\beta_i + \beta_\infty = 1$) containing information about the restriction of the depolarizing processes, as indicated in the previous section. As discussed later, since $\phi_1 \ll \phi_2 \ll \phi_3$, the fastest correlation time (ϕ_1) can be assigned to the wobbling of the fluorescein dye (ϕ_L), the intermediate one (ϕ_2) to overall restricted taxoid reorientation (ϕ_T), and the slowest (ϕ_3) to the depolarization produced by energy transfer ($\langle\phi_{ET}\rangle$). The parameters P_{2L}, P_{2T}, and P_{2ET} from eqs 7 and 8 are most simply expressed in terms of the β_i and β_∞ as

$$P_{2L}{}^2 = 1 - \beta_1 \qquad (13)$$

$$P_{2T}{}^2 = \frac{1 - \beta_1 - \beta_2}{1 - \beta_1} = \frac{\beta_\infty(f\rightarrow 0)}{1 - \beta_1} \qquad (14)$$

$$P_{2ET}{}^2 = \frac{\beta_\infty(f\rightarrow 1)}{1 - \beta_1 - \beta_2} = \frac{\beta_\infty(f\rightarrow 1)}{\beta_\infty(f\rightarrow 0)} \qquad (15)$$

where the central expression in eq 14 applies in both the saturated and low-labeling regimes. Further details of the modeling of the anisotropy decay are given in the following section.

Table 1: Spectral Properties of Flutax1 and Flutax2 Free (in PEGTA Buffer) and Bound to Microtubules (MT-I)[a]

sample	pH	$\lambda_{max}{}^{abs}$ (nm)	$\lambda_{max}{}^{em}$ (nm)[b]	$\epsilon(\lambda_{max})$ ($\mathrm{M^{-1}\,cm^{-1}}$) (±5000)	Φ[c] (±0.05)
Flutax1	6.5	495	527	52000[d]	0.60
Flutax1	9.0	497	527	78000	0.80
Flutax2	6.5	496	526	80000	0.90
Flu1-Ala	9.0	497	527	73000	0.80
Flutax1/MT-I	6.5	497	523	60000[e]	0.80
Flutax2/MT-I	6.5	498	523	67000	0.90

[a] [Flutax] = 2 μM; Flutax:$\alpha\beta$-tubulin, 1:10; 37 °C. [b] Corrected fluorescence spectra. [c] Average fluorescence quantum yield, $\lambda^{ex} = 470 \pm 2$ nm. [d] Effective molar absorption coefficient of the equilibrium mixture of fluorescein mono- and dianion species. [e] Error estimate: $\pm 10^4$ $\mathrm{M^{-1}\,cm^{-1}}$.

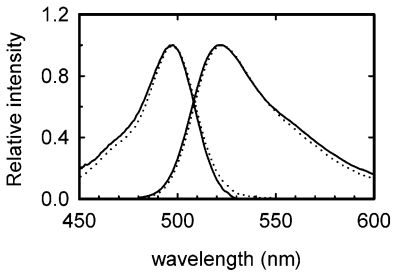

FIGURE 2: Normalized absorption and corrected fluorescence spectra of 2 μM Flutax1 [7-*O*-[*N*-(fluorescein-4′-carbonyl)-L-alanyl]-taxol] (—) and Flutax2 [7-*O*-[*N*-(2,7-difluorofluorescein-4′-carbonyl)-L-alanyl]taxol] (···) bound to microtubules (MT-I) at low molar labeling ratio (flutax:$\alpha\beta$-tubulin, 1:10) in PEGTA buffer, pH 6.5, 37 °C, and $\lambda^{ex} = 470$ nm. Efficient transfer of excitation energy between identical dye molecules, at labeling ratios close to saturation, is due to the overlap between absorption and emission spectra.

RESULTS

Spectral Properties of Flutax Free and Bound to Microtubules. The absorption and fluorescence spectroscopic parameters of Flutax1 and Flutax2 free in buffer solution and bound to the microtubule protein lattice in MT-I preparations are summarized in Table 1, as well as those of the inactive derivative Flu1-Ala. The shape and intensity of the absorption and fluorescence spectra of Flutax1 in solution (Figure 2) depend strongly on pH, due to the different properties of the two prototropic species, mono- and dianion, of the appending fluorescein dye. The fluorescence and absorption spectra of the two species in Flutax1 are almost the same as those of the free dye, the only difference being a small red shift in the dianion absorption spectra (3 and 7 nm in PEDTA and PEGTA buffers, respectively). The pK_a of the fluorescein group of Flutax1, as determined in PEGTA buffer from absorption and fluorescence measurements, is 6.33 ± 0.05, also coincident with that of the free dye in aqueous solution, 6.37 ± 0.07 (*38, 47*), indicating the absence of strong electrostatic interactions between the appending dye and Taxol domains.

The data of Table 1 for Flutax1 free in solution at pH 6.5 correspond to the equilibrium mixture of the two anionic forms of the dye. The low absorption coefficient and

Table 2: Fluorescence Lifetimes and Anisotropy Decay Parameters of Flutax1 and Flutax2 Bound to Microtubules (MT-1 and MT-II) as a Function of the Taxoid:αβ-Tubulin Molar Ratio from High Dilution ($f \rightarrow 0$) to Saturation ($f \rightarrow 1$)[a]

sample	τ (ns) (±0.05)	β_1[b] (±0.02)	ϕ_1[b] (ns) (±0.1)	β_2 (±0.01)	ϕ_2 (ns) (0.8−3)[c]	β_3 (±0.01)	$\langle\phi_{ET}\rangle$[d] (ns)	β_4 (±0.01)	r_∞[e] (±0.01)	$\bar{r}$[f] (±0.01)
Flutax1[g]	4.05	0.61	0.24	0.39	0.9 (0.6−1.7)					0.04
Flutax/MT-I, 1:1000 to 1:10	4.01	0.25	0.2	0.10	1.5	0.65[h]			0.25	0.27
Flutax1/MT-I, 1:1	4.13	0.39	0.2	0.10	1.5	0.36	14 (12−17)	0.15	0.06	0.18
Flutax2/MT-I, 1:1	4.02	0.34	0.2	0.19	1.5	0.34	8 (6−12)	0.13	0.05	0.16
Flutax1/MT-II, 1:1	4.19	0.36	0.2	0.19	1.5	0.30	14 (12−17)	0.15	0.06	0.17

[a] [TB] = 20 μM; 37 °C. [b] Rotational correlation times (ϕ_i) and fractional contributions (β_i) from the analysis of the anisotropy decay. [c] Confidence intervals corresponding to 1 standard deviation. [d] Average correlation time due to energy transfer depolarization. [e] Limiting value of the anisotropy at long times. [f] Steady-state anisotropy, $\lambda^{ex} = 440$ nm, $\lambda^{em} = 520$ nm. [g] Data for the free taxoid in PEGTA buffer, pH = 8, 37 °C, $\eta = 1.5$ cP, was included here for comparison. [h] At low saturation there is no significant energy transfer and therefore $\beta_3 \equiv \beta_\infty$.

fluorescence yield of Flutax1 in these conditions are due to the presence of the monoanion species, with $\epsilon^{mono}_{m,490nm} = 16425\ M^{-1}\ cm^{-1}$ and $\Phi^{mono} = 0.36$ (*38*). In the case of Flutax2 the acidity of the fluorine-substituted dye (Scheme 1) is much higher than that of the parent fluorescein, pK_a 4.81 (*48*), and therefore the dianion is essentially the only emitting species present in these conditions.

The fluorescence decay of a solution of Flutax1 at pH 6.5, excited at $\lambda^{ex} < 470$ nm, also reveals the presence of both mono- and dianion. Thus, for example, the decay at $\lambda^{ex} = 460$ nm can only be adequately fitted to a biexponential function, with lifetimes (fractional preexponentials) of 3.2 ± 0.1 ns (0.3) and 4.05 ± 0.05 ns (0.7). The two lifetimes correspond to the fluorescein mono- and dianion species, respectively, as in the free dye, and are independent of pH, taxoid concentration (0.2−2 μM), and buffer composition. The relative weights of the preexponential terms, indicated in parentheses above for pH 6.5, depend on pH and agree closely with those computed, taking into account the equilibrium concentrations of the two forms. The fluorescence decay of solutions of Flutax2 in the two buffers mentioned above is monoexponential, also having a lifetime τ of 4.05 ns, which is independent of pH and excitation wavelength, as expected.

Interestingly, when Flutax1 is bound to microtubules, the absorption and emission spectra, as well as the fluorescence yield, of the appending dye correspond to the *dianion* species, with a 4 nm blue shift characteristic of the bound dianion emission (Table 1). In the case of Flutax2 the bound form is also the dianion, which is the only species present in solution, and exhibits a similar 3 nm blue shift. All of the spectral parameters presented above are very similar for both microtubule preparations MT-I and MT-II.

The fluorescence decay time of the taxoids bound to microtubules is, again, ca. 4.05 ns and does not depend on the excitation wavelength, buffer composition, or microtubule preparation. This observation confirms that the only species of the bound Flutax1 emitting is the dianion. In this case, apparently, strong electrostatic interactions of the tubulin surface with the complex stabilize the doubly charged species, competing effectively with the acidity of the surrounding buffer and facilitating the study of the liganded system. In all of these samples, a minor (<5%) component with a short lifetime (1 ± 0.5 ns) can frequently be observed, which arises from residual inactive taxoid impurities (*32*).

Fluorescence Depolarization of Flutax Bound to Microtubules at Low Labeling Ratio ($f \rightarrow 0$). The fluorescence emission of the taxoid free in solution is depolarized due to rotational motions of the complex as a whole and to independent oscillations of the appended dye. However, when the taxoid is bound to microtubules, a large increase in the emission anisotropy is observed. A representative trace of the fluorescence anisotropy decay of Flutax 1 in solution is shown in Figure 3, where it can be observed that the anisotropy decreases first from a large initial value $r_0 = r(0) = 0.39$ with a subnanosecond time constant, followed by a second, slower, well-separated depolarization process; Flutax2 exhibits the same biphasic decay.

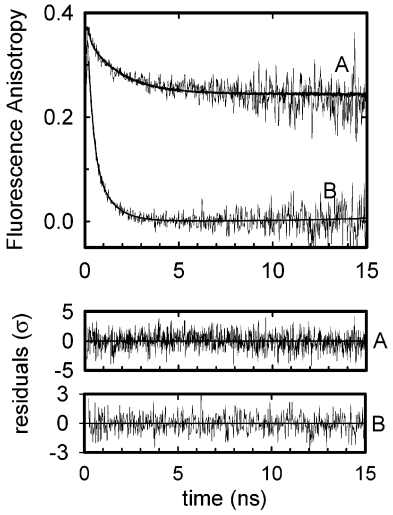

FIGURE 3: (A) Decay of the fluorescence anisotropy of 20 nM Flutax1 bound to microtubules (MT-I) at low molar labeling ratio (1:1000 Flutax:αβ-tubulin) in PEGTA buffer, pH 6.5, 37 °C, λ^{ex} 497 nm, and λ^{em} 520 nm. (B) Fluorescence anisotropy decay of free taxoid in the same buffer, for comparison (20 nM, pH 8). The global fit to the parameters listed in Table 2 is shown as solid lines, with the randomly distributed weighted residuals due to deviations of the data from the fit presented in the lower panel.

The subnanosecond rate was assigned (Cañadas et al., to be published) to the independent oscillation of the linked dye (ϕ_L), while the slower rate represents the Brownian rotation of the taxoid molecule as a whole (ϕ_T). The data of Table 2 register the best-fit parameters for these two dynamic processes for a PEGTA solution of Flutax1 at 37 °C, pH 8. A large fraction (β_1), accounting for ~60% of the anisotropy, is averaged by the rapid restricted motion of the appending dye, with a correlation time ϕ_1 of ~200 ps. The remaining fraction, represented by the value of $r_{\infty L} = r_0(1 - \beta_1) = 0.15$, is finally randomized by taxoid molecular rotations with a correlation time ϕ_2 of ~1 ns.

When Flutax1 is bound to the microtubule surface in MT-I samples, at low concentration far from saturation ($f \rightarrow 0$),

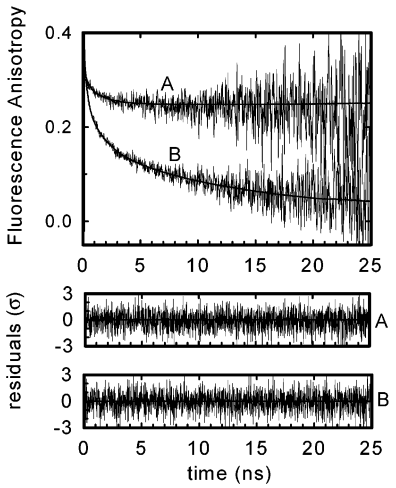

FIGURE 4: Homotransfer depolarization of Flutax1 bound to microtubules. (A) In Flutax/MT-I samples with low Flutax:αβ-tubulin molar labeling ratio (1:10) there is no energy transfer, and the anisotropy decays due to the conformational flexibility of the complex to a constant value $r_\infty = 0.25$. (B) In Flutax-saturated samples (molar ratio 1:1) a new anisotropy decay mode is observed, with a relaxation time of 14 ns, due to homotransfer of excitation between neighbor taxoids. [Flutax1] = 2 μM in PEDTA buffer, pH 6.6, 37 °C, λ^{ex} 440 nm, and λ^{em} 520 nm. The solid line indicates the fit to the anisotropy parameters listed in Table 2, with the random distribution of the weighted residuals shown in the lower panel.

the stationary anisotropy increases from the free solution value of 0.04 to 0.27. This increase is due to the restrictions of the bound taxoid fluctuations, as can be appreciated in the time-resolved traces (Figure 3); the corresponding best-fitting parameters to eq 12 are listed in Table 2. By comparison of the data in Table 2 for free and bound Flutax1 at $f \rightarrow 0$, it can be seen that (i) the value of the fluorescein subnanosecond wobbling rate ϕ_1 does not change significantly on binding, whereas the amplitude of this motion is strongly reduced, (ii) the global motion of the taxoid in the microtubule surface ϕ_2 is slowed and its amplitude largely suppressed, and (iii) in the bound taxoid there is a large fraction of residual anisotropy (r_∞) that remains constant within the observation time.

These changes in the anisotropy parameters of Flutax1 when bound to microtubules are fully reversible, as can be determined by adding to a sample of bound Flutax1 the nonemitting drug docetaxel, which binds to microtubules and displaces Flutax1 back into solution with ~90% efficiency (*29*). The anisotropy parameters of Flutax1 after the addition of docetaxel (data not shown) are very similar to those of the free taxoid.

Fluorescence Depolarization of Flutax Bound to Microtubules in Saturating Conditions ($f \rightarrow 1$) by Homogeneous Resonance Energy Transfer (FREHT). When the amount of Flutax bound to microtubules reaches saturation, i.e., there is one liganded taxoid for each αβ-tubulin heterodimer in the microtubule, the decay of the fluorescence anisotropy shows a new depolarizing process (Figure 4), and a lower value of r_∞, the anisotropy at long times, despite the fact that none of the remaining spectroscopic parameters (in particular, the fluorescence lifetime) are affected. This pattern can be observed for both of the two taxoid derivatives in both MT-I and MT-II preparations. The new depolarizing factor was assigned to resonance energy transfer between identical dye molecules that in these conditions are held in close proximity by the microtubule structure. This assignment is supported by the dependence of the steady-state emission anisotropy, $\bar{r}$, on the excitation wavelength: for excitation energies within the red edge of the absorption band, $\bar{r}$ increases with increasing wavelength as the energy transfer efficiency decreases (*49*). Thus, for MT-I saturated with Flutax1 (1:1 Flutax1:αβ-tubulin molar ratio), the steady-state anisotropy increases from $\bar{r} = 0.18 \pm 0.01$ ($\lambda^{ex} = 440$ nm) to $\bar{r} = 0.24 \pm 0.02$ ($\lambda^{ex} = 510$ nm). By contrast, the same preparation with a 1:1000 molar ratio, where no significant FREHT will occur, exhibits a steady-state emission anisotropy $\bar{r} = 0.27 \pm 0.02$, which is independent of the excitation wavelength over the whole of this range.

The analysis of the anisotropy decay traces in the presence of energy transfer was carried out with the simplest model, that incorporating a third depolarizing time constant representing an average correlation time $\langle\phi_{ET}\rangle$ for the FREHT-induced depolarization and the appropriate new residual anisotropy term $r_{\infty ET}$, to the two correlation times discussed above (ϕ_1 and ϕ_2) for the low-labeled samples. A "global" approach was employed (see Materials and Methods) that consists first in the simultaneous analysis of all the anisotropy decay curves for preparations with low taxoid labeling ratios (1:1000−1:10 taxoid:αβ-tubulin molar ratio), in which no energy transfer is present (Table 2). In a second step, the taxoid-saturated samples were individually analyzed according to the model indicated above. In this analysis, the number of adjustable parameters was reduced on the assumption that, within the 67% confidence limits for the low-labeled samples, the correlation times ϕ_1 and ϕ_2 were independent of the extent of saturation and of the much longer FREHT correlation time. Their values were consequently set at those found by the global analysis of the data for the low-labeled samples (Table 2). The associated preexponential terms β_1 and β_2, as well as β_3 corresponding to β_∞ in the low-labeled samples, were allowed to adjust freely in the analysis. This is justified by the range of their values found in individual low-labeled samples, much wider than the 67% confidence limits on the globally analyzed data (Table 2). These may arise partly from the presence of small amounts of inactive but fluorescent taxoid, forming aggregates or associated (nonspecifically) to residual unassembled tubulin, as well as of larger amounts of active taxoid in equilibrium with the bound form for ($f \rightarrow 1$) MT samples. In addition, one cannot exclude subtle differences in the MT structure between the $f \rightarrow 0$ and $f \rightarrow 1$ conditions.

The first effects were corrected by taking into account an estimated ~1.5% presence of inactive fluorescent taxoid and ~6% of unbound active fluorescent taxoid (*32*). A doubling of the estimate for the unbound active taxoid, while somewhat altering the individual values of β_3 and β_4 from those listed in Table 2, did not make any significant difference to the final result for the parameters of FREHT-induced depolarization, i.e., neither to the correlation time $\langle\phi_{ET}\rangle$ nor to the ratio of β_3 and β_4 upon which the determination of the polar angle γ, which partially governs the FREHT rate, depends.

These analyses yielded identical $r_{\infty ET}$ values but different average correlation times for FREHT-induced depolarization, ~14 ns for Flutax1 and ~8 ns for Flutax2 (Table 2). This difference is expected for such an energy transfer process

Table 3: Polar Angle, γ, and Estimated Limits for the Orientation Factor $\langle\kappa^2\rangle$ and Förster Radii R_0 (Å) for Energy Transfer between Nearest-Neighbor Flutax Pairs Bound to a Microtubule Made of $N = 14$ Protofilaments[a]

transfer pair	γ[b] (deg)	$\langle\kappa^2\rangle_{min}$[c]	$\langle\kappa^2\rangle_{max}$[c]	$R_{2/3}$ (±0.7)	R_{0min} (±1)	R_{0max} (±1)
Flutax1−Flutax1	33 ± 2	0.33 (±0.02)	0.71 (±0.02)	43.6	39	44
Flutax2−Flutax2	33 ± 2	0.33 (±0.02)	0.71 (±0.02)	46.7	42	47

[a] Errors due to sample-to-sample variability. [b] Orientation of the mean position of the transition moment of the fluorescent group with respect to the long axis of the microtubule from two microtubule preparations, MT-I and MT-II, and both of the fluorescent taxoids. [c] The extreme values of $\langle\kappa^2\rangle$ are set, for the values of γ found here, by the maximum and minimum values (0 and $\pi/2$) of the azimuth ψ (see Appendix).

Table 4: Separation, R, between Two Nearest-Neighbor Taxoid Molecules Bound to Microtubules of $N = 12$ and $N = 14$ Protofilaments As Determined from Experimental Homotransfer Depolarization Rates

	$N = 14$			$N = 12$[a]		
		taxoid−taxoid separation (Å)			taxoid−taxoid separation (Å)	
taxoid	R/R_0	R_{max}	R_{min}	R/R_0	R_{max}	R_{min}
Flutax1	0.95 (0.92−0.98)[b]	42 ± 2	37 ± 2	1.00 (0.98−1.03)	44 ± 2	39 ± 2
Flutax2	0.87 (0.83−0.93)	41 ± 2	36 ± 2	0.912 (0.87−0.96)	43 ± 2	38 ± 2

[a] The geometrical differences between the $N = 14$ and $N = 12$ structures do not result in significant changes in the orientation parameters (cf. Table 3). [b] Sample-to-sample variability.

on consideration of the different spectral characteristics of the two fluorescein dyes (overlap integral and quantum yield) and, therefore, larger characteristic Förster radius for Flutax2 as compared with Flutax1 (vide infra).

Determination of Taxoid−Taxoid Separations from FREHT-Induced Depolarization. The values of the preexponential terms β_i, the correlation time $\langle\phi_{ET}\rangle$, and the residual anisotropy $r_{\infty ET}$ in the taxoid-saturated samples are determined by the structure of the microtubule with the taxoid bound and the separation of the emitting ligands. A model of the FREHT process in the microtubule was developed (see Appendix) that predicts the values for the time-resolved depolarization parameters as a function of the relative orientation and separation of the fluorescein groups of nearest-neighbor bound taxoids, in a ring perpendicular to the symmetry (long) axis of the MT. Together with the spectroscopic data for the probes, these could then be interpreted quantitatively in terms of nearest-neighbor separation and consequently the radial location of the bound taxoids.

Polar Angle γ and Förster Radius R_0. Using eq 10 and the molar absorption coefficients for Flutax1 and Flutax2 dianions, for pH 9 and pH 6.5, respectively (Table 1), the spectral "self"-overlap integrals, J, were determined to be $(5.6 \pm 0.6) \times 10^{14}$ and $(7.5 \pm 0.5) \times 10^{14}$ M^{-1} cm^{-1} nm^4, respectively. The characteristic Förster radii R_{0max} and R_{0min}, calculated from eq 11 and used in interpretation of the FREHT depolarization data, depend on the maximum and minimum values of $\langle\kappa^2\rangle$ determined by the specific geometry of the fluorophore array on the microtubules and the extent and rate of local restricted reorientation of the fluorophores. The expression for $\langle\kappa^2\rangle$ given by eq A2 can be recast in terms of two of the FREHT model parameters determined experimentally, the polar angle γ and the depolarization factor $\langle d^x\rangle$:

$$\gamma = \cos^{-1}\left(\sqrt{\frac{1}{3} + \frac{2}{3}\sqrt{\frac{\beta_4}{\beta_3 + \beta_4}}}\right) \qquad (16)$$

$$\langle d^x\rangle = P_{2L}P_{2T} = \sqrt{\frac{r_{\infty T}}{r_0}} = \sqrt{1 - \beta_1 - \beta_2} \qquad (17)$$

together with a single unknown parameter, the azimuth ψ (Figure 6). The important angle γ is that formed by the mean orientation of the electronic transition moment of the fluorescein molecule with the microtubule long axis. From the experimental β_3 and β_4 values (Table 2) one gets $\gamma = 33 \pm 2°$, noting that both taxoids adopt the same orientation γ with respect to the symmetry axis of the microtubule and the same azimuth ψ when bound to the microtubule wall.

The unknown azimuth ψ leads to uncertainties in $\langle\kappa^2\rangle$ for any particular donor−acceptor pair in the array, which are in general smaller the smaller the polar angle. Maximum and minimum values of $\langle\kappa^2\rangle$ for nearest-neighbor pairs were calculated using eq A2, with $\langle d^x\rangle = 0.70 \pm 0.03$ and $\gamma = 33 \pm 2°$. The resulting $\langle\kappa^2\rangle_{max}$ and $\langle\kappa^2\rangle_{min}$ values, corresponding for the relevant range of γ to azimuths ψ of 0 and $\pi/2$, respectively, were used finally to compute the R_{0max} and R_{0min} extrema. All of these parameters, together with the standard $R_{2/3}$ value, are presented in Table 3.

Nearest-Neighbor Separation and Diameter of Taxoid Binding Site Helix. The separation between nearest-neighbor fluorescein molecules (R) can be obtained from the experimental values of R_0, the FREHT (one way) rate constant k_{ET}, and the fluorescence lifetime of the dye by means of eq A1. k_{ET} is just the inverse of the experimental average correlation time $\langle\phi_{ET}\rangle$ for FREHT-induced depolarization in the 14-membered ring model multiplied by a constant which depends on the polar angle γ (see eq A9). Using the extrema R_{0max} and R_{0min} (Table 3), together with the Flutax lifetimes and average FREHT-induced correlation times given in Table 2, the maximum and minimum nearest-neighbor separations, R_{max} and R_{min}, were calculated as

$$R_{max,min} = R_{0max,min}\sqrt[6]{\frac{\langle {c_{1+2}}^{-1}\rangle^{-1}\langle\phi_{ET}\rangle}{\tau}} \qquad (18)$$

and are presented in Table 4. The maximum and minimum nearest-neighbor separations are very consistent both between the two different fluorophores and the different MT preparations, approximating overall ~41 ± 3 and ~36.5 ± 3 Å, respectively.

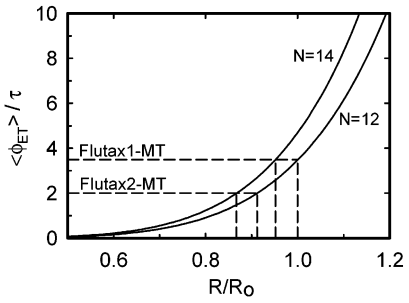

FIGURE 5: Average energy transfer depolarization time constant $\langle\phi_{ET}\rangle$ as a function of the bound Flutax−Flutax separation (R) for microtubules (MT) with $N = 12$ and $N = 14$ protofilaments and a value of the mean transition inclination γ of 33°. The continuous lines were computed with the microtubule ring model described in the text, and both parameters are shown divided by the fluorescence lifetime τ and the characteristic Förster distance R_0, respectively, to make the plot independent of the spectral properties of the dye. The dashed lines mark the separation corresponding to the experimental $\langle\phi_{ET}\rangle$ values for Flutax1 (14 ns) and Flutax2 (8 ns), with a common fluorescence lifetime of 4.05 ns. The uncertainty introduced in the R/R_0 value by this protofilament variability is only ∼5%.

This separation between Flutax molecules bound to the microtubule wall uniquely determines the maximum and minimum diameters, D_{max} and D_{min}, possible for the helix (as approximated by those of the ring in the model used), which are then obtained as ∼184 ± 13 and ∼164 ± 14 Å from

$$D_{max,min} = R_{max,min}/\sin(\pi/14) \qquad (19)$$

Considering the otherwise known dimensions of the microtubule, these values are compatible only with a location of the fluorescent taxoids close to the inner wall of the microtubule.

As mentioned above, the dominant population of microtubules saturated with Flutax contains 14 protofilaments (*32*). Nevertheless, significant fractions of microtubules with $N = 12$ and $N = 13$ protofilaments may also be present, which might be a source of uncertainty in the estimation of the taxoid−taxoid separation by FREHT. This uncertainty was determined here by solving the ring model for different values of N. The model predictions for $N = 12$ and $N = 14$ protofilaments, with $\gamma = 33°$, are compared in Figure 5, which shows the expected depolarization relaxation time due to energy transfer $\langle\phi_{ET}\rangle$ as a function of the taxoid−taxoid separation R in the two microtubule structures (actually Figure 5 shows $\langle\phi_{ET}\rangle/\tau$ as a function of R/R_0, to make the plot independent of the dye spectroscopic parameters).

In the case of Flutax1, for example, the experimental value of $\langle\phi_{ET}\rangle = 14$ ns corresponds to R/R_0 values of 1.0 and 0.95 for microtubules with 12 and 14 protofilaments, respectively, which translate to taxoid−taxoid maximum separations of 44 and 42 Å (Table 4). Therefore, the presence of different polymorphs with 12−14 protofilaments would not affect the conclusion arrived at here as to the location of the taxoid in the inner wall of the microtubule.

DISCUSSION

Changes in the Fluorescence Parameters of Flutax Derivatives upon Binding to Microtubules. The spectral changes of Flutax analogues that result from interaction with the microtubule binding site report on the microenvironment of the parent drug Taxol, because both the "dark" parent and the fluorescent analogue have a common MT binding center (*24*, *29*). In the case of Flutax1, large increases in the fluorescence intensity and the anisotropy are observed when it binds to microtubules suspended in slightly acidic buffers (pH ∼6.5). The data presented here conclusively show that the increase in the fluorescence intensity is due to selective occupation of the β-tubulin taxoid site by the highly fluorescent dianion form of Flutax1, in contrast with the equilibrium mono/dianion mixture in the surrounding buffer. Since the difluorofluorescein group of Flutax2 (Scheme 1) is present only in the dianion form in the same solution, a small blue shift of the fluorescence maximum is the only change, apart from the anisotropy increase, that is observed on binding of this analogue. The preferential stabilization of the doubly charged species by the protein lattice requires a positive electrostatic potential to interact with the negative phenolate charge of the dye (*50*).

On the other hand, the single-exponential fluorescence lifetime of the bound dianion was found to be independent of the extent of ligand occupation of the microtubule binding site, indicative of a homogeneous interacting surface or, in other words, of a single class of binding sites, in the concentration range explored here. Otherwise, multiple lifetimes would be observed, due to the sensitivity of the excited-state kinetics to the microenvironment of the fluorophore.

Because the spectroscopic parameters of the dianion are not substantially affected by its interaction with the microtubule wall, the increase in fluorescence polarization observed on Flutax binding can only be due to consequent mechanical restrictions on the mobility of the taxoid. Dissection of these dynamic changes necessitated picosecond time resolution and shows that, in addition to the expected restriction of the Brownian rotational tumbling of the taxoid as a whole on docking, the local independent oscillations of the fluorescein xanthene ring in the 200 ps range almost disappear. In fact, a large fraction of the increase in polarization following binding is due to the abrogation of this ultrafast motion. On the other hand, the anisotropy data (Table 2) indicate that the interacting protein surface does not totally prevent conformational fluctuations of the bound taxoid which, in addition, should be exposed to the bulk solvent if the rapid interchange between active taxoids is to be explained (*8*, *32*). The oscillations of the xanthene ring in bound Flutax can be presented in a more intuitive way as linear excursions of that ring by the expression (Cañadas and co-workers, in preparation): $\langle\cos\theta\rangle_{rms} = [(2/3)[r_\infty/r_0] + (1/3)]^{1/2}$.

The values of $\langle\cos\theta\rangle_{rms}$ for the fast (∼200 ps) and slow (1.5 ns) motions of bound Flutax, computed from the data in Table 2, are 0.91 and 0.96, respectively, corresponding to root-mean-square lateral fluctuations of the fluorescein ring of 1−3 Å. Interestingly, values in this range are frequently postulated for the lateral mobility of amino acid side chains in flexible protein domains (*51*).

The fluorescent properties of Flutax bound to microtubules discussed above define a surface of interaction in the microtubule that shares several common features with a model of the Taxol binding center proposed recently (*52*).

In this model, which results from fitting a T-shaped Taxol conformation to the high-resolution structure of $\alpha\beta$-tubulin, the C7 position of the taxane ring projects away from the central region of the β-tubulin subunit toward the inter-protofilament space, such that it abuts a highly hydrophilic segment of the M-loop. This segment contains two protonated arginine residues of which one can be at interaction distance from substituents at that position in the taxane ring, as proposed before (*19b*, *32*), thus stabilizing the Flutax1 dianion form. In contrast, this interaction is not as obviously attainable in the case of alternative orientations of the bound taxoids, rotated 180° end-on, which have also been postulated (*20*, *28*). To explain the variability in the number of microtubule protofilaments (*11*) and the rapid switching between protofilament numbers induced by the taxoids (*8*), that part of the protofilament contact surface must have important conformational flexibility.

The Flutax−Flutax Separation in the Microtubule. When microtubules are fully saturated with either of the Flutax derivatives (1:1 taxoid:$\alpha\beta$-tubulin molar ratio), a new relaxation time is observed in the decay of the fluorescence anisotropy, which differs by an order of magnitude from those discussed above. The new depolarization process was assigned to homogeneous resonance electronic energy transfer (FREHT) between neighboring Flutax molecules, which gives rise to randomization of the fluorescence polarization down to a low residual value of the anisotropy ($r_{\infty ET}$). From this last parameter it is possible to estimate the mean inclination γ of the emitting dye transition moment relative to the long axis of the microtubule. However, to determine analytically the separation of the taxoid molecules, a model of the tubulin lattice of the microtubule is required. We have demonstrated here that the $1/R^6$ dependence of the energy transfer rate assists in the simplification of the model, which is adequately representable by a single circular section of the microtubule, i.e., a ring of 12 or 14 tubulin $\alpha\beta$-dimers each associated with a bound taxoid, appreciable energy transfer occurring only between neighboring molecules within the ring.

The geometry of the ring model departs from reality only in one aspect: all the tubulin molecules are in the same plane, whereas in the helical arrangement of the actual microtubule there is a vertical shift of ~40 or 80 Å between the first and the last tubulin β-units in the ring, depending on whether the lattice at that point is A or B, respectively (*53*). Nevertheless, the difference introduced by this shift, or by the occasional presence of discontinuities (seams) in the tubulin lattice (*7*, *11*), will not appreciably affect the separation values determined here (Table 4). Another possible complication might be the presence of sheetlike arrays of protofilaments at the open ends of microtubules (*53*). The depolarization induced in them by FREHT would be negligible, due to the near parallel orientation of the dye molecules in such sheets.

Analytical solution of the coupled homotransfer equations for this tubulin ring model without further approximations is direct but somewhat tedious. In this way, the mean inclination γ of the fluorophore to the microtubule axis was found to be $33 \pm 2°$, and a Flutax−Flutax nearest-neighbor separation of 40 ± 5 Å obtained, independent of the Flutax derivative used (Flutax1 and Flutax2) and of the microtubule preparation (MT-I and MT-II).

Location of the Taxol Binding Site in the Microtubule Wall. Microtubules, as mesoscopic objects, are readily visualized in relatively high detail (*1*), and it is therefore simple to translate the Flutax−Flutax separation given by the energy transfer measurements into a location of the taxoid on the microtubule diameter. Taking 165 and 265 Å for values of the microtubule internal and external diameters (*4*, *22c*), one can predict that the maximum separation between Flutax molecules if located at the external surface would be ~60 Å. Similarly, the minimum value at the internal surface would be ~37 Å. Thus, the unique location of the Flutax (and therefore Taxol) binding site consistent with the value of the Flutax−Flutax separation measured here (40 ± 5 Å) is close to the inside surface of the microtubule, even allowing for the length of the spacer between the fluorophore and taxoid frame.

Current inferences as to the location of the taxoid binding pocket in the microtubule are mostly based on an $\alpha\beta$-tubulin structure that has gradually been refined, from 6 to 5, 4, 3.7, and, most recently, 3.5 Å resolution (*22*). These structures were obtained from electron crystallography of two-dimensional arrays of tubulin polymerized in the presence of zinc ions, in which protofilaments align in an antiparallel way, as compared with parallel alignment for microtubules in cells and in the zinc-free solutions employed in the present study. The resulting structure of the protein was finally docked into the microtubule using density maps obtained by cryoelectron microscopy, with 20 Å (*3*) and 14 Å (*4*) resolution. In the final microtubule structure, the taxoid binding pocket faces the interior space of the tubule, lying in a region of the β-tubulin subunit at the interface between adjacent protofilaments and close to the wide pores in the lattice. The taxoid−taxoid separation that can be estimated from these images (~43 Å) is in very good accord with the FREHT value measured here.

On the other hand, as noted in the introduction, recent direct measurements of the binding rate of Flutax derivatives to preassembled microtubules yielded values of $\sim 10^6$ M^{-1} s^{-1} for the corresponding bimolecular rate constant (*32*). To explain these high diffusion rates, it was postulated that the $\alpha\beta$-tubulin dimers might be rotated axially in the protofilament, exposing the binding site to the bulk solution. The new evidence provided here on the Flutax−Flutax separation by energy transfer experiments makes this possibility very unlikely. We rather consider that the location of the Taxol-interacting pocket in the microtubule lumen and the above kinetic results can be made compatible by the presence of channels (pores) connecting the external and lumenal surfaces (*2*), with estimated diameters of up to ~25 Å according to the reconstructed microtubule structures (*4*). Simple arguments lead to estimates of $\sim 10^9$ M^{-1} s^{-1} for the diffusion rate constant in aqueous solution of a molecule of the size of Flutax (diameter 15−20 Å) to the surface of an infinite tubulin wall. Since the fraction of that surface corresponding to the empty channels is, at least, ~10%, the rate constant of diffusion to the pore entrance would be $\sim 10^8$ M^{-1} s^{-1}. Finally, it is not unrealistic (see, e.g., ref *54*) that hindered diffusion through the pores of the tubulin lattice may reduce the overall rate by a further factor of 10^2, accounting for the observed overall value of $\sim 10^6$ M^{-1} s^{-1}. Moreover, we speculate that taxoid flow from the bulk solution to the inner microtubule surface may be further facilitated by the internal

microtubule dynamics (*8*), which is required to explain the fairly rapid addition and loss of protofilaments triggered by taxoids, this dynamic process being envisaged as the formation of transient microdefects in the tubulin lattice, or the opening and closing of seams along the microtubule wall (*8*).

CONCLUSIONS

It has been shown here that the microtubule binding site of Taxol exhibits a neat selectivity for the dianion form of the fluorescein moiety in Flutax1. This selectivity and the presence of residual taxoid fluctuations within its binding pocket (1−3 Å), determined by time-resolved anisotropy measurements, reinforce the idea of a bound taxoid in which the C7 position of the molecule is close to a positively charged segment of the flexible M-loop in the β-tubulin subunit of the microtubule. The spectroscopic observations are more consistent with the protein binding surface fitted to the T-conformation of the bound drug proposed recently (*52*), rather than with other previous alternative tubulin−taxoid interacting surfaces.

The nearest-neighbor Flutax−Flutax separation in taxoid-saturated microtubules takes a value of 40 ± 5 Å, as measured by resonance energy homotransfer experiments, that is only possible if the taxoid binding site is located very close to the internal surface of the microtubule. To reconcile this observation with the known fast diffusion of Flutax to its binding center, large (>25 Å) openings are required to be present in the tubulin lattice making up the microtubule. Since Flutax and the parent drug have the same tubulin active center, the above results represent an experimental determination of the position of the Taxol binding site in microtubules in solution.

ACKNOWLEDGMENT

We thank Drs. Francisco Amat-Guerri, A. A. Souto, and E. Quesada for the preparation of the fluorescent taxoids and Drs. G. Rivas and A. Evangelio for valuable help in sample preparation. This contribution is dedicated to the memory of Dr. F. W. John Teale.

APPENDIX

Homogeneous Resonance Energy Transfer and Fluorescence Depolarization in a Symmetrical Ring of Identical Fluorophores: A Model for Flutax Bound at Saturation to the Taxoid Binding Sites of Microtubules. (A) Förster Long-Range Resonance Excitation Energy Transfer. When the emission spectrum of a fluorophore overlaps with the absorption spectrum of another, and individual molecules of the two (donor and acceptor) species are close enough together, the excitation energy may be transferred from donor to acceptor by a direct dipole−dipole coupling mechanism, as first fully formalized by Förster (*55*): Förster resonance energy transfer, or FRET (*56*). The same process may occur between two like fluorophores, which are close enough together, because of the self-overlap between their absorption and emission spectra (Förster resonance energy homotransfer, FREHT). In this case, however, multiple retransfers will occur, the excitation energy being localized alternately on each partner until emission or another deactivation process occurs in one or the other of the two excited states (*55a*). In both cases, the one-way rate of resonance energy transfer is given by

$$k_{ET} = \frac{1}{\tau_{0D}}\left(\frac{R_0}{R}\right)^6 \qquad \text{(A1)}$$

where τ_{0D} is the donor excited-state lifetime in the absence of energy transfer and R is the separation between donor and acceptor. R_0 is the characteristic Förster separation at which energy transfer to the acceptor competes equally with the other excited-state deactivation processes and close to which the transfer efficiency measurement is most sensitive to variation in the donor−acceptor separation.

In general, both donor and acceptor transition moments will have some restricted reorientational freedom which can reasonably be modeled as cylindrically symmetric about some mean orientation (see Theory). Under these conditions, if the restricted reorientation is rapid with respect to the transfer rate, a dynamic average of κ^2 (*57*) can be defined for *homotransfer* as

$$\langle\kappa^2\rangle = \kappa^{x2}\langle d^x\rangle^2 + {}^2/_3(1 - \langle d^x\rangle) + (\cos^2\Theta_D + \cos^2\Theta_A)\langle d^x\rangle(1 - \langle d^x\rangle) \qquad \text{(A2)}$$

where $\kappa^{x2} = (\cos\Theta_{DA} - 3\cos\Theta_D\cos\Theta_A)^2$, with Θ_{DA}, Θ_D, and Θ_A defined on the mean orientations of the donor and acceptor transition moments with respect to each other and to the separation vector, and the Soleillet depolarization factor $\langle d^x\rangle = {}^3/_2\langle\cos^2\theta^x\rangle - {}^1/_2$ describes the rapidly averaging restricted orientational distribution of the transitions about their mean orientation, here identical for the donor absorption and acceptor emission transitions.

In the case of FREHT, donor−acceptor transfer is fully reversible, and in contrast with cases of partially reversible transfer between unlike fluorophores (*58*), the excitation energy is shared equally at long enough times and/or transfer rates high enough with respect to the (common) de-excitation rate. Just as in the irreversible case with fluorescent acceptor, such a transfer will also, in general, lead to depolarization of the emission of an acceptor relative to that of the initially excited fluorophore, as quantitated by Förster (*55a*) for the isolated pair case. The process can take place over many like fluorophores that are serially close enough together, and as elaborated below for the present case, the emission of the ensemble as a whole is thus depolarized.

(B) Application to a Model of the Flutax−Microtubule System. In this model, we assume that all the fluorophores are spectroscopically identical and situated in identical local environments at the tubulin binding sites. In particular, they exhibit the same absorption and emission spectra, excited-state lifetime (monoexponential decay), and quantum yield. Under these conditions, the FREHT process does not modify the overall excited-state decay or quantum yield of the fluorophores. In addition, they are each characterized by the same extent of rapid restricted reorientation. The fluorophores are thus considered as being distributed in groups of the number of binding sites per helical turn of the microtubule. These sites are regularly spaced around the circumference of diameter D inscribed in a plane perpendicular to the long axis of the microtubule, each group being separated from others above and/or below by the $\alpha\beta$-tubulin protofilament

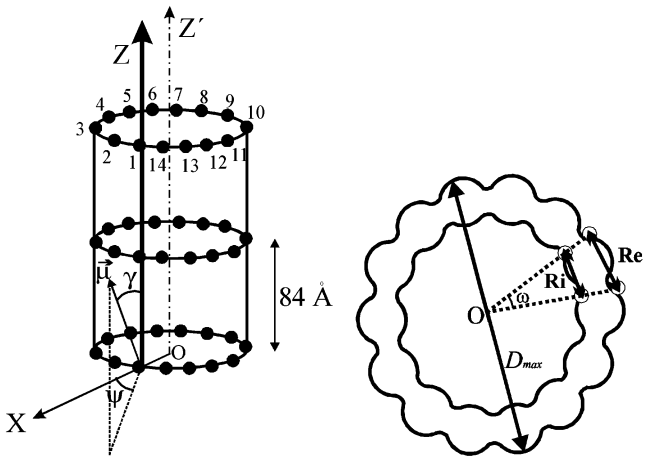

FIGURE 6: (a) Idealization of the microtubule lattice as a regular cylinder built of 14 αβ-tubulin heterodimer protofilaments parallel to the microtubule axis, Z', with no vertical shift between adjacent protofilaments. Structurally, this corresponds to a series of stacked 14-membered αβ-tubulin heterodimers symmetrically arranged as hollow rings oriented with their planes perpendicular to the microtubule axis. Bound taxoid molecules at saturation of sites, pictured as filled circles, are cylindrically symmetrically distributed around the circumference of each disk, the disk being a cross-section through each ring at the level of the binding site. The vertical disk-to-disk separation corresponds to the heterodimer−heterodimer spacing in the protofilaments. $\vec{\mu}$ represents the transition moment of one of the bound Flutax molecules, γ being the angle between this and the local vertical axis Z parallel to the microtubule axis, while ψ is the corresponding azimuthal angle in the perpendicular plane, i.e., the plane of the disk. For clarity of presentation, the αβ-tubulin subunits themselves are not represented. (b) Section through the 14-membered αβ-tubulin heterodimer ring of the model presented in (a), showing the axial symmetry of the system ($\omega = \pi/7$) and the relationship between taxoid−taxoid separation and microtubule diameter.

heterodimer vertical dimension. We select here a 14-membered ring of fluorophores, corresponding to a full helical turn in the microtubule (Figure 6).

Only the saturated site case is considered. The mean orientation of each fluorophore is taken to be identically disposed with respect to its local frame, which is described by the radius vector of the circle and the tangent at its intersection with the circumference. The separation for next-nearest neighbors in each ring is thus almost twice that between nearest ones. The one-way transfer rate between them, being proportional to the inverse sixth power of their separation, will thus be less than 2% of that for the nearest neighbors and, to a good approximation, can safely be neglected. The process of forward and reverse transfer between the two nearest neighbors of any given excited fluorophore, whether it has received its energy by absorption of incident light or via energy transfer, will serially migrate the excitation energy backward and forward around the ring. The probability of any particular fluorophore being excited at very long times in a ring thus tends toward (1/14). The competing processes of emission and radiationless deactivation may take place at any time during this step-by-step migration process. The light thus emitted is, in general, depolarized with respect to that emitted from the initially excited fluorophore by a degree dependent on whether it is nearest, next-nearest, or further neighbor to the initially excited fluorophore. The depolarization of light emitted by

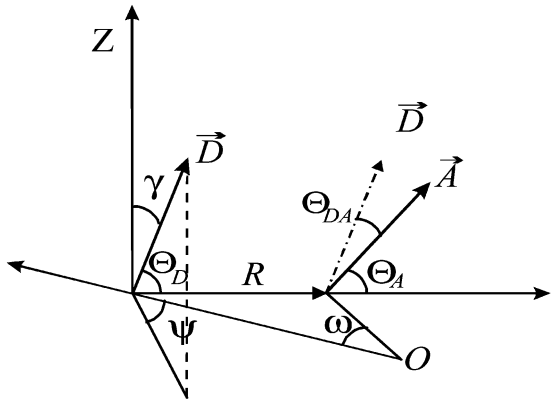

FIGURE 7: Transition moment orientations of nearest-neighbor bound Flutax donor (D) and acceptor (A) molecules showing the relationship between the standard representation of the orientation factor κ^{x2} defined by eq A2 and the cylindrical coordinate system angles γ, ψ, and ω.

the nth such neighbor remains identical whether that fluorophore had previously transferred its excitation energy and subsequently received it back after a shorter or longer excursion onto its nearest and further neighbors. It should be noted that the spacing of fluorophores aligned immediately above and below along the length of the microtubule (Figure 6) is also much greater than the nearest-neighbor separation within each ring (or each turn of the microtubule helix), so the rate of direct transfer in the "vertical" direction is negligible, too. Even if it were not, however, such transfers would not produce any difference in the observed depolarization, as the orientations are identical unless the alignment is imperfect.

Under the further assumption, borne out in the present experimental case, that the depolarization rate due to FREHT is much slower than that due to restricted reorientation of the fluorophore, the FREHT depolarization of fluorescence of the nth nearest neighbor, i.e., the depolarization other than that caused by restricted reorientation, is constant. It is characterized by the depolarization factor $\langle d_{Tn}\rangle = {}^3/_2\langle\cos^2\Theta_{DAn}\rangle - {}^1/_2$, Θ_D and Θ_{An} are separated by the azimuth $n\omega = n(\pi/7)$, and both transition moments are oriented at the polar angle γ to the symmetry axis which is perpendicular to the ring (Figures 6 and 7). Thus:

$$\cos\Theta_{DAn} = \cos^2\gamma + \sin^2\gamma\cos(n\pi/7) \qquad \text{(A3)}$$

In the microtubule system, γ is the inclination of the long molecular axis of the fluorescein moiety in the taxoid to the microtubule axis (Z-axis) and determines the maximum extent of depolarization at long times in that system. For example, at $\gamma = 0°$ (long axis of fluoresceins parallel to the microtubule axis), no FREHT-induced depolarization would occur, while for $\gamma = 54.7°$ (magic angle), the depolarization would be complete ($r_\infty = 0$). As will be shown below, it is quite straightforward to obtain the value of γ from the experimental values of $r_{\infty T}$ and $r_{\infty ET}$, though over the upper part of its angular range a given depolarization factor ≤ 0.25 derived therefrom corresponds to two different values of γ either side of the magic angle. In the present case, it turns out that this possibility is not encountered (see Results).

There are two identical neighbors at each of the nearest to 6th nearest separations, and one 7th nearest neighbor, in

a 14-membered ring. The time-dependent FREHT depolarization factor is the average of the constant depolarization factors over the evolving probabilities of excited-state occupation of the originally excited site and its neighbors. As indicated above, each position is equally represented at long enough times, leading to a constant (time-infinity) factor directly reflecting the orientation γ of the mean transition moment with respect to the axis of symmetry of the microtubule. The evolution of excitation probability for each of the nth nearest neighbors under the assumption of interaction only between nearest neighbors with a one-way rate constant k_{ET} is obtained as the solution of the simultaneous rate equations:

$$-\frac{dp_0(t)}{dt} = \left(\frac{1}{\tau} + 2k_{ET}\right)p_0(t) - 2k_{ET}p_1(t) \qquad \text{(A4)}$$

$$-\frac{dp_n(t)}{dt} = \left(\frac{1}{\tau} + 2k_{ET}\right)p_n(t) - k_{ET}[p_{n-1}(t) + p_{n+1}(t)] \quad (n = [2, 6]) \qquad \text{(A5)}$$

$$-\frac{dp_7(t)}{dt} = \left(\frac{1}{\tau} + 2k_{ET}\right)p_7(t) - 2k_{ET}p_6(t) \qquad \text{(A6)}$$

with initial conditions $p_0(0) = 1$, $p_n(0) = 0$ ($n = [1, 7]$) and final conditions $p_n(t \rightarrow \infty) = {}^1/_{14}$ ($n = 0$ and 7), $p_n(t \rightarrow \infty) = {}^1/_7$ ($n = [1, 6]$). The overall (summed) excited-state decay remains monoexponential with lifetime τ, while on constructing the time dependence of depolarization due to FREHT from the evolution of each of the n species and the constant FREHT depolarization factors for them, all but three of the kinetic terms for depolarization are identically zero, leaving

$$\frac{3}{2}\langle\cos^2\Theta_{DAn}\rangle - \frac{1}{2} = b_1\exp[-c_1k_{ET}t] + b_2\exp[-c_2k_{ET}t] + b_3 \qquad \text{(A7)}$$

where $b_1 = {}^3/_4\sin^4\gamma$, $b_2 = 3\sin^2\gamma\cos^2\gamma$, $b_3 = ({}^3/_2\cos^2\gamma - {}^1/_2)^2$, $c_1 = 0.753020$, and $c_2 = 0.198062$. The ratio $c_1/c_2 \approx 3.802$ approaches that of 4 pertaining to the analogous expression describing depolarization arising from uniaxial Brownian rotation (*59*).

Under the above assumption of restricted rotational depolarization much more rapid than that due to energy transfer, the overall time-dependent FREHT depolarization at times t long compared with the local restricted reorientational depolarization (eq 8 in main text) may be represented to a good approximation in terms of emission anisotropy by

$$r_M(t)(f\rightarrow 1) = r_0P_{2L}{}^2P_{2T}{}^2\left\{\frac{3}{2}\langle\cos^2\Theta_{DAn}\rangle(t) - \frac{1}{2}\right\} \approx r_0P_{2L}{}^2P_{2T}{}^2\left\{(1 - P_{2ET}{}^2)\exp\left[-\frac{t}{\langle\phi_{ET}\rangle}\right] + P_{2ET}{}^2\right\} \qquad \text{(A8)}$$

where ($f \rightarrow 1$) indicates saturation of binding sites. P_{2ET} identifies with b_3, and its experimental value thus determines γ. The time-dependent depolarization factor in eq A8 is entirely analogous to that given previously (*59*, *60*) for the specific case of an excited fluorophore "jump-diffusing" between three symmetrically oriented positions. As shown in ref *60*, its form is independent of the number (≥ 3) of fluorophores symmetrically disposed around the ring. The general solution for the anisotropy decay given there (*60*) was not readily adaptable by us to the present case, and specific solutions were therefore obtained here as described above.[2]

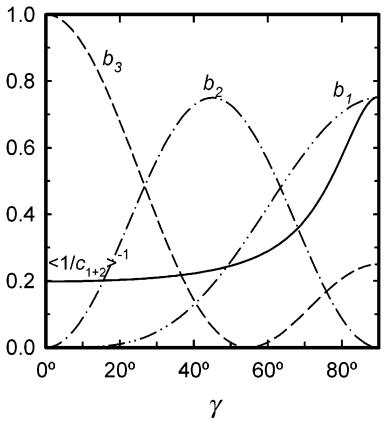

FIGURE 8: Geometrical factors b_1, b_2, and b_3 appearing in the full and approximate time-dependent FREHT depolarization factors, together with the weighted average numerical multiplier, $c_2 = 0.198062 \leq \langle 1/c_{1+2}\rangle^{-1} \leq c_1 = 0.753020$, of k_{ET}, defined in eq A7 and appearing in the approximation ($N = 14$).

As seen by comparing eqs A7 and A8, $\langle\phi_{ET}\rangle$ represents an average correlation time for the FREHT depolarization process defined for an initial partial anisotropy $(b_1 + b_2) = {}^3/_4\sin^2\gamma(1 + 3\cos^2\gamma)$ and constant area under the decay:

$$\langle\phi_{ET}\rangle = \left(\frac{1}{1 + 3\cos^2\gamma}\right)\left(\frac{\sin^2\gamma}{c_1} + \frac{4\cos^2\gamma}{c_2}\right)\frac{1}{k_{ET}} = \left\langle\frac{1}{c_{1+2}}\right\rangle\frac{1}{k_{ET}} = \left\langle\frac{1}{c_{1+2}}\right\rangle\tau_{0D}\left(\frac{R}{R_0}\right)^6 \qquad \text{(A9)}$$

The preexponential factors b_1, b_2, and b_3, together with the harmonically averaged coefficient $c_1 \geq \langle 1/c_{1+2}\rangle^{-1} \geq c_2$ of k_{ET} (i.e., the apparent average rate coefficient $\langle\phi_{ET}\rangle^{-1}$ normalized to unit FREHT transfer rate), are presented as functions of γ in Figure 8.

It is noted that if $\gamma < \cos^{-1}[(2/3)^{1/2}] \approx 35.26°$ (as in the present case, where $\gamma = 33 \pm 2°$), its value is uniquely determined by b_3. In addition, for this range of γ and smaller, the average coefficient of k_{ET} contains less than a 12% contribution from c_1, leading to very good monoexponential approximations to the full biexponential time-dependent part of the FREHT-induced depolarization (see Results).

(C) Interpretation of the FREHT Rate, k_{ET}. In terms of γ and the local azimuth ψ of the mean orientation of the transition moments with respect to the radius vector in the plane perpendicular to the symmetry axis (Figure 6), the angular parameters appearing in $\langle\kappa^2\rangle$, defined in eq A2, are

$$\cos\Theta_D = \sin\gamma\cos\left(\frac{3\pi}{7} + \psi\right) \qquad \text{(A10)}$$

$$\cos\Theta_A = \sin\gamma\cos\left(\frac{4\pi}{7} + \psi\right) \qquad \text{(A11)}$$

[2] Only the final result describing this model will be given here. A more complete treatment of such systems, including lower membered rings, will be presented elsewhere (M. P. Lillo, R. E. Dale, and A. U. Acuña, manuscript in preparation).

along with that in eq A3. Whereas γ is experimentally defined, the azimuth ψ is unknown. Knowledge of the relevant average orientation factor is thereby restricted to maximum and minimum possible values. Within the range of γ up to about 35°, however, as in the present case (see Results), the maximum value is given for $\psi = 0$ and the minimum for $\psi = \pi/2$.

REFERENCES

1. Dustin, P. (1984) *Microtubules*, 2nd ed., Springer-Verlag, New York.
2. Amos, L. A., and Klug, A. J. (1974) *J. Cell Sci. 14*, 523−549.
3. Nogales, E., Whittaker, M., Milligan, R. A., and Downing, K. H. (1999) *Cell 96*, 79−88.
4. Meurer-Grob, P., Kasparian, J., and Wade, R. H. (2001) *Biochemistry 40*, 8000−8008.
5. Mandelkow, E.-M., Mandelkow, E., and Milligan, R. A. (1991) *J. Cell Biol. 114*, 977−991.
6. Tilney, L. G., Brian, J., Bush, D. J., Fujiwara, K., Mooschker, M. S., Murphy, D. B., and Snyder, D. H. (1973) *J. Cell Biol. 59*, 267−275.
7. (a) Wade, R. H., Chrétien, D., and Job, D. (1990) *J. Mol. Biol. 212*, 775−786; (b) Chrétien, D., and Fuller, D. (2000) *J. Mol. Biol. 298*, 663−676.
8. Díaz, J. F., Valpuesta, J. M., Chacón, P., Diakun, G., and Andreu, J. M. (1998) *J. Biol. Chem. 273*, 33803−33810.
9. Longford, J. M. (1980) *J. Cell Biol. 87*, 521−526.
10. Andreu, J. M., Bordás, J., Díaz, J. F., García de Ancos, J., Gil, R., Medrano, F. J., Nogales, E., Pantos, E., and Town-Andrews, E. (1992) *J. Mol. Biol. 226*, 169−184.
11. Chrétien, D., and Wade, R. H. (1991) *Biol. Cell 107*, 161−174.
12. Wani, M. C., Taylor, H. L., Wall, M. E., Coggon, P., and McPhail, A. T. (1971) *J. Am. Chem. Soc. 93*, 2325−2327.
13. Nicolau, K. C., Dai, W.-M., and Guy, R. K. (1994) *Angew. Chem., Int. Ed. 33*, 15−44.
14. Horwitz, S. B. (1994) *Ann. Oncol. 5* (Suppl. 6), 3−6.
15. Rowinsky, E. K., and Donehower, R. C. (1995) *N. Engl. J. Med. 332*, 1004−1013.
16. Parness, J., and Horwitz, S. B. (1981) *J. Cell Biol. 91*, 479−487.
17. Díaz, J. F., and Andreu, J. M. (1993) *Biochemistry 32*, 2747−2775.
18. Caplow, M., Shanks, J., and Ruhlen, R. (1994) *J. Biol. Chem. 269*, 2399−2402.
19. (a) Rao, S., Horwitz, S. B., and Ringel, I. (1992) *J. Natl. Cancer Inst. 84*, 785−788; (b) Rao, S., Lifeng, H., Chakrawarty, S. Ojima, I., Orr, A., and Horwitz, S. B. (1999) *J. Biol. Chem. 274*, 37990−37994.
20. Combeau, C., Commerçon, A., Mioskowski, C., Rosseau, B., Aubert, F., and Goeldner, M. (1994) *Biochemistry 33*, 6676−6683.
21. Dasgupta, D., Haeil, P., Harriman, G., Georg, G., and Himes, R. H. (1994) *J. Med. Chem. 37*, 2976−2980.
22. (a) Nogales, E., Wolf, S. G., Khan, I. A., Ludueña, R. F., and Downing, K. H. (1995) *Nature 375*, 424−427; (b) Nogales, E., Wolf, S. G., and Downing, K. H. (1997) *J. Struct. Biol. 118*, 119−127; (c) Nogales, E., Wolf, S. G., and Downing, K. H. (1998) *Nature 391*, 199−203; (d) Löwe, J., Li, H., Downing, K. H., and Nogales, E. (2001) *J. Mol. Biol. 313*, 1045−1057.
23. Dye, R. B., William, R. J., Jr. (1996) *Biochemistry 35*, 1433−1439.
24. Abal, M., Souto, A. A., Amat-Guerri, F., Acuña, A. U., Andreu, J. M., and Barasoain, I. (2001) *Cell Motil. Cytoskeleton 49*, 1−15.
25. Souto, A. A., Acuña, A. U., Andreu, J. M., Barasoain, I., Abal, M., and Amat-Guerri, F. (1995) *Angew. Chem., Int. Ed. 34*, 2710−2712.
26. Guy, R. K., Scott, Z. A., Sloboda, R. D., and Nicolau, K. C. (1996) *Chem. Biol. 3*, 1021−1031.
27. Sengupta, S., Borge, T. C., Liu, Y., Hepperle, M., George, G. I., and Himes, R. H. (1997) *Biochemistry 36*, 5179−5184.
28. Li, Y., Poliks, B., Cegelski, L., Poliks, M., Gryczynski, Z., Grzegorz, P., Jagtap, P. G., Studelska, D. R., Kingston, D. G. I., Schaefer, J., and Bane, S. (2000) *Biochemistry 39*, 281−291.
29. Evangelio, J. A., Abal, M., Barasoain, I., Souto, A. A., Lillo, M. P., Acuña, A. U., Amat-Guerri, F., and Andreu, J. M. (1998) *Cell Motil. Cytoskeleton 39*, 73−90.
30. Andreu, J. M., and Barasoain, I. (2001) *Biochemistry 40*, 11975−11984.
31. Jiménez-Barbero, J., Souto, A. A., Abal, M., Barasoain, I., Evangelio, J., Acuña, A. U., Andreu, J. M., and Amat-Guerri, F. (1998) *Bioorg. Med. Chem. 6*, 1857−1863.
32. Díaz, J. F., Strobe, R., Engelborghs, Y., Souto, A. A., and Andreu, J. M. (2000) *J. Biol. Chem. 275*, 26265−26276.
33. Soleillet, P. (1929) *Ann. Phys. 12*, 23−97.
34. Restall, C. J., Dale, R. E., Murray, E. K., Gilbert, C. W., and Chapman, D. (1984) *Biochemistry 23*, 6765−6766.
35. Dale, R. E., and Eisinger, J. (1975) in *Biochemical Fluorescence: Concepts* (Chen, R. F., and Edelhoch, H., Eds.) Vol. I, pp 115−284, Marcel Dekker, New York.
36. Steiner, R. F. (1991) in *Topics in Fluorescence Spectroscopy* (Lakowicz, J. R., Ed.) Vol. 2, pp 1−52, Plenum Press, New York.
37. Stryer, L. (1978) *Annu. Rev. Biochem. 47*, 819−846.
38. Klonis, S., and Sawyer, W. H. (1996) *J. Fluoresc. 6*, 145−157.
39. Andreu, J. M., Díaz, J. F., Gil, R., de Pereda, J. M., García de Lacoba, M., Peyrot, V., Briand, C., Towns-Andrews, E., and Bordás, J. (1994) *J. Biol. Chem. 269*, 31785−31792.
40. Weber, G., and Teale, F. W. J. (1956) *Trans. Faraday Soc. 53*, 646−655.
41. Heller, C. A., Henry, R. A., McLaughlin, B. A., and Bliss, D. E. (1974) *J. Chem. Eng. Data 19*, 214−219.
42. Blumberg, W. E., Dale, R. E., Eisinger, J., and Zuckerman, D. M. (1974) *Biopolymers 13*, 1607−1620.
43. Teale, F. W. J. (1969) *Photochem. Photobiol. 10*, 363−374.
44. Oldenbourg, R., Salmon, E. D., and Trau, P. T. (1988) *Biophys. J. 74*, 645−654.
45. Sato, H., Ellis, G. W., and Inouè, S. (1975) *J. Cell Biol. 67*, 501−517.
46. Beechem, J. M., Gratton, E., Ameloot, M., Knutson, J. R., and Brand, L. (1991) in *Topics in Fluorescence Spectroscopy* (Lakowicz, J. R., Ed.) Vol. 2, pp 241−305, Plenum Press, New York.
47. Sjöback, R., Nygren, J., and Kubista, M. (1995) *Spectrochim. Acta, Part A 51*, L7−L21.
48. Sun, W. C., Gee, K. R., Klaubert, D. H., and Haugland, R. P. (1997) *J. Org. Chem. 62*, 6469−6475.
49. Weber, G., and Shinitzky, M. (1970) *Proc. Natl. Acad. Sci. U.S.A. 65*, 823−830.
50. Fompeydie, D., Rabaron, A., Levillain, P., and Bourdon, R. (1981) *J. Chem. Res.*, 4052−4061.
51. Karplus, M., and Petsko, G. A. (1990) *Nature 347*, 631−639.
52. Snyder, J. P., Nettles, J. H., Cornett, B., Downing, K. H., and Nogales, E. (2001) *Proc. Natl. Acad. Sci. U.S.A. 98*, 5312−5316.
53. Chrétien, P., Fuller, S. D., and Karsenti, E. (1995) *J. Cell Biol. 129*, 1311−1328.
54. Nitsche, J. M., and Balgi, G. (1994) *Ind. Eng. Chem. Res. 33*, 2242−2247.
55. (a) Förster, Th. (1948) *Ann. Physik 2*, 55−75; (b) Förster, Th. (1965) in *Modern Quantum Chemistry* (Sinanolu, O., Ed.) Part III, pp 93−137, Academic Press, New York.
56. Van Der Meer, B. W., Coker, G., III, and Simon Chen, S.-Y. (1994) *Resonance Energy Transfer*, VCH Publishers, New York.
57. Dale, R. E., Eisinger, J., and Blumberg, W. E. (1979) *Biophys. J. 26*, 161−194.
58. (a) Porter, G. B. (1972) *Theor. Chim. Acta 24*, 265−270; (b) Wooley, P., Steinhauser, K. G., and Epe, B. (1978) *Biophys. Chem. 26*, 367−374.
59. Wahl, Ph. (1975) in *Biochemical Fluorescence: Concepts* (Chen, R. F., and Edelhoch, H., Eds.) Vol. I, pp 1−41, Marcel Dekker, New York.
60. Gottlieb, Yu. Ya., and Wahl, Ph. (1963) *J. Chim. Phys. 60*, 849−856.

BI0261793